



Available online at www.sciencedirect.com

ScienceDirect

Advances in Space Research 61 (2018) 2290–2300

ADVANCES IN
SPACE
RESEARCH
(a COSPAR publication)
www.elsevier.com/locate/asr

Inter-satellite calibration of FengYun 3 medium energy electron fluxes with POES electron measurements

Yang Zhang^{a,*}, Binbin Ni^a, Zheng Xiang^a, Xianguo Zhang^{b,c}, Xiaoxin Zhang^d,
Xudong Gu^a, Song Fu^a, Xing Cao^a, Zhengyang Zou^a

^a Department of Space Physics, School of Electronic Information, Wuhan University, Wuhan, Hubei, China

^b Laboratory of Space Environment Exploration, National Space Science Center, Chinese Academy of Sciences, Beijing, China

^c Beijing Key Laboratory of Space Environment Exploration, Beijing, China

^d Key Laboratory of Space Weather, National Center for Space Weather, China Meteorological Administration, Beijing, China

Received 10 October 2017; received in revised form 9 January 2018; accepted 15 February 2018

Available online 2 March 2018

Abstract

We perform an L-shell dependent inter-satellite calibration of FengYun 3 medium energy electron measurements with POES measurements based on rough orbital conjunctions within $5 \text{ min} \times 0.1 \text{ L} \times 0.5 \text{ MLT}$. By comparing electron flux data between the U.S. Polar Orbiting Environmental Satellites (POES) and Chinese sun-synchronous satellites including FY-3B and FY-3C for a whole year of 2014, we attempt to remove less reliable data and evaluate systematic uncertainties associated with the FY-3B and FY-3C datasets, expecting to quantify the inter-satellite calibration factors for the 150–350 keV energy channel at $L = 2\text{--}7$. Compared to the POES data, the FY-3B and FY-3C data generally exhibit a similar trend of electron flux variations but more or less underestimate them within a factor of 5 for the medium electron energy 150–350 keV channel. Good consistency in the flux conjunctions after the inter-calibration procedures gives us certain confidence to generalize our method to calibrate electron flux measurements from various satellite instruments.

© 2018 COSPAR. Published by Elsevier Ltd. All rights reserved.

Keywords: Inter-satellite calibration; Medium energy electron flux; L-dependent adjustment factors; Fengyun-3 satellites; Earth's radiation belts

1. Introduction

The Earth's electron radiation belt is characteristically highly dynamic, due to an imbalance between various source and loss processes (e.g., Reeves et al., 2003; Thorne et al., 2005; Ni et al., 2013, 2015, 2018; Baker et al., 2014; Xiang et al., 2016, 2017; Cao et al., 2017). Dynamic variations in the natural energetic electron environment can impact space hardwares and contribute significantly to the background signals in a range of flown

instruments (Friedel et al., 2002, 2005). Information derived from multiple instruments in space has traditionally been used to establish statistical models and study the radiation belt dynamics (e.g., Thorne, 2010; Thorne et al., 2013). Before further applications can be investigated, a basic requirement is the availability of the multi-satellite data that has been calibrated properly. Nowadays, existing instrument calibrations often range from comprehensive to nonexistent, while detailed calibrations are always expected to be preferentially performed for instruments from the same satellite series (Friedel et al., 2005). While there has been much progress in the modeling of energetic particle instruments, those methods have their own challenges (Cayton and Tuszezski, 2005). To recover

* Corresponding author.

E-mail addresses: kwzhangyang@whu.edu.cn, 793955571@qq.com (Y. Zhang).

the clean spectrum from an instrument, given the limitations of each individual instrument's calibrations, we try to resort to further on-orbit calibrations with the available collected data. Inter-satellite calibration can be referred as such a method, since it is basically based on observations as opposed to theoretical or modeling estimates. Using data derived from multi-satellites (e.g., CRRES, LANL GEO, Polar) that covers a period of three full solar cycles, Friedel et al. (2005) conducted a statistical inter-calibration of magnetospheric electron data. Using the static OP77 magnetic field model (Olson and Pfitzer, 1977), they also established a common geomagnetic coordinate system for all the satellites and then got a statistically meaningful set of electron flux conjunctions to calculate the feasible adjustment factors between any two instruments. Chen et al. (2005) implemented the calibration method based on obtaining electron phase space density (PSD) conjunctions at fixed values of phase space coordinates (PSCs) between three LANL GEO satellites for a geo-magnetically quiet period. Ni et al. (2009a,b, 2011) adopted a similar approach to perform cross-satellite calibrations based on PSD conjunctions between the satellite pairs of CRRES/Akebono, CRRES/LANL GEO and THEMIS/LANL. In this study, we will present the procedure used for the inter-satellite calibration of FengYun 3 (short for FY-3 hereinafter) with already corrected POES electron measurements.

The NOAA POES mission consists of a series of sun synchronous satellites orbiting at the altitude of ~ 800 km, covering a broad range of MLT sectors and L-shells with an orbital period of ~ 100 min. The Space Environment Monitor (SEM-2) instrument package onboard these satellites have two electron solid-state detector telescopes that measure electron fluxes in three energy bands (>30 , >100 , >300 keV) (Evans and Greer, 2004; Green, 2013). The 0° -pointing detectors are mounted on the three-axis stabilized POES spacecraft so that the center of each field of view is outward along the local zenith, while another set of telescopes, termed the 90° detectors, are mounted approximately perpendicular to the 0° detector. Through the complex electrical signal (produced by particles) processing, the two detectors can provide the precipitating electron fluxes and trapped (including quasi-trapped) electron fluxes. The 0° detector measures the precipitating particle fluxes inside the bounce loss cone at $L > 1.4$ (Rodger et al., 2010) with a field view of $\pm 15^\circ$ centered along the local zenith, and the 90° telescope that is mounted approximately perpendicular to the former with the same field of view mostly measures trapped and quasi-trapped particles over the invariant latitude range between 55° and 68° ($\sim L = 3\text{--}7$ in a dipole field) (Meredith et al., 2011). Readers are referred to the study of Evans and Greer (2004) for a detailed description of POES detectors and the mechanism of the energetic electron measurements.

FY-3B and FY-3C were launched in November 2011 and September 2013 respectively into the solar synchronization orbit at an altitude of ~ 830 km with an inclination

of 98° and an orbit period of ~ 90 min. FengYun satellites carry a SEM with two detectors onboard to measure the intensities of the ions and electrons precipitating into the upper atmosphere. The charged particles impact the sensors through the light-blocking layer and the collimator. These particles settle in the sensors and generate electric pulses. The amplitude and anticoincidence of these pulses can be used to identify the particle type and energy. Both satellites have the High Energy Electron Detector (HEED) with a large field view of 40° that is capable of monitoring the electron dynamics of five energy channels (0.15–0.35 MeV, 0.35–0.65 MeV, 0.65–1.2 MeV, 1.2–2.0 MeV, and 2.0–5.7 MeV). The detector mainly measures the trapped energetic electron fluxes, as it is mounted perpendicular to the plane of the satellite trajectory (Huang et al., 2012; Wang et al., 2010, 2013; Li et al., submitted for publication). Readers are referred to the studies of Huang et al. (2012) and Li et al. (2017) for more details of the capabilities and applications of FY-3B and FY-3C Space Environment Monitor (SEM) on monitoring space weather events.

The reminder of the paper is outlined as follows. In Section 2, we give a brief description of the satellite data used and also present the general procedure of obtaining the requisite data sets from conjunctions. In Section 3, we evaluate the inter-satellite calibration factors at different L-shells for both satellites: FY-3B and FY-3C. In Section 4, we discuss our results and make conclusive remarks.

2. Data availability

To calibrate the electron data derived from the FY-3 probes, it is necessary to use the best available data that has been corrected as the standard. Similar to the FY-3 orbits, the sun-synchronous POES satellites fly at the altitude of ~ 800 km around every 100 min. In our study, we use the POES 100–300 keV trapped electron fluxes (obtained by subtracting the fluxes of the >300 keV channel from those of the >100 keV channel) (Li et al., 2013; Ni et al., 2014) to calibrate the FY-3 150–350 keV trapped electron fluxes. The general data processing procedure is described as follows:

Firstly, the data contamination should be carefully dealt with. The measurements are likely to be contaminated by enhanced background counts. To make the data sets as clean as possible, following the correction procedure described by Lam et al. (2010), we remove the proton contamination from POES electron measurements. As of the FY-3 electron data, the portion of proton contaminated datasets is actually quite small and has little influence on the analysis results. In addition, we need to avoid the measurements from both satellite series during the solar proton events and in the region of the South Atlantic anomaly (SAA) (Casadio and Arino, 2011).

Secondly, the background levels should be subtracted from the original data. The background levels are present in all particle instruments, resulting from the thermal noise,

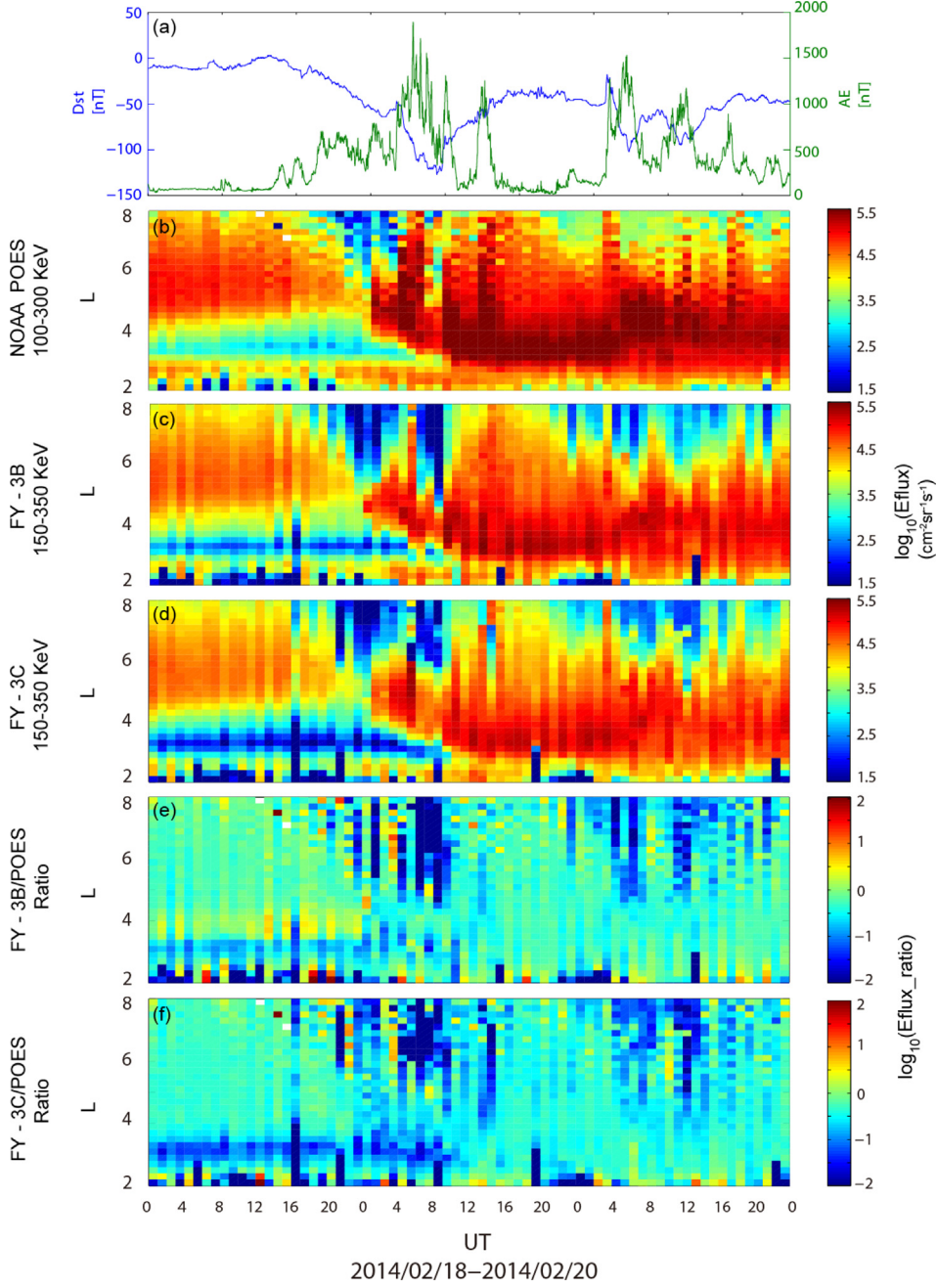


Fig. 1. Temporal variations of radiation belt electron flux observed by low-altitude FY-3B and FY-3C spacecraft and NOAA POES series and the FY-3-to-POES flux ratios during the 3-day storm time period.

the cosmic rays and so on. We can study and track these background levels following Friedel et al. (2005). Generally, this correction is small since the real count rates are much higher than the background levels. However, it becomes necessary when the count rates are very low. In this paper, we select reasonable threshold values for the considered medium energy channel through a detailed statistical analysis, as will be described in Section 3.

Ideally, a strict conjunction is defined on basis of the actual locations of two spacecrafts within a very small distance interval, which however is very hard to find and thus substantially limits the number of conjunctions. Thus,

through pursuing relatively more relaxed conjunction bin within $0.5 \text{ MLT} \times 0.1 \text{ L} \times 5 \text{ min}$, we can obtain a statistically useful set of conjunctions between FY-3 and POES electron measurements. In our definition of the conjunction, the constraint on L is the most restrict condition that requires the satellite measurements to be very close to the same drift shell, while the limits on MLT and UT ulteriorly help us get relatively more precise conjunctive points over space and time. Once we have collected a bunch of conjunctions, through detailed statistical investigation, an adjustment factor can be calculated for each L-shell of interest.

3. Analysis results

3.1. Inter-calibration method

In the present study, we utilize data derived from five POES satellites (i.e., NOAA (15, 16, 18, 19), and MetOp-02) and two FY-3 probes (i.e., FY-3B and FY-3C). Fig. 1 displays an example of trapped electron fluxes measured by the two low-altitude series of satellites for a 3-day period from 18 to 20 February 2014. Fig. 1a shows the temporal variations of the Dst index and the AE index based on the OMNIWeb data sets. During the 3-day interval, sharp changes existed in the two parameters, presenting a prolonged geomagnetic storm and intervals of sub-storms. Binned by 0.2 L-shell with a time resolution of 1 h, the flux variations are displayed from Fig. 1b to d, respectively, showing a similar trend of temporal evolution with the strong electron flux enhancements occurring remarkably during the long-time storm period. Most of the ratios shown in the bottom two panels of Fig. 1 range from 0.1 to 10, indicating the rough consistency in the electron measurements of both satellite series at the considered middle-energy channel, while it is worthwhile to note that the FY-3 measurements more or less tend to be lower than the POES measurements.

Following the procedures described in Section 2, we first search for satellite conjunctions within the bin size of 0.5 MLT \times 0.1 L \times 5 min. In order to get high-quality data, we remove the conjunctions for which the FY-3 data has less than five points. Fig. 2 presents three conjunction event examples between FY-3B and MetOp-02 at different L-shells, which are randomly selected as good examples to illustrate our practice of obtaining standard data sets

from conjunctions. Each subplot means a conjunction that contains the basic referenced POES flux (blue line), the corresponding FY-3 fluxes within the 5-min time bin (hollow points attached to the red dashed line) and the averaged FY-3 flux (red solid line). We then combine the basic POES flux and the averaged FY-3 flux as a data set for each conjunction to establish the overall database of all the conjunctions. Fig. 2 also indicates that the ratio of the POES flux to the averaged FY-3 flux tends to vary largely with L-shell, which justifies our attempts to estimate the adjustment factors as a function of L-shell.

As pointed out above, it is necessary to reduce the effect of the background noises. Fig. 3 shows the overall number distribution of the conjunction events as a function of the FY-3-to-POES flux ratio at different flux ranges. It is evident that the electron measurements of FY-3 are smaller than those of POES for the considered medium energy channel in most instances. To pursue a reliable analysis of the distribution feature of conjunctions, the conjunctions are divided into other five groups based on POES fluxes of different orders of magnitude (i.e., $0\text{--}10^2$, $10^3\text{--}10^4$, $10^4\text{--}10^5$, $>10^5$) for comparisons. Note that most of the ratios (>10) are present in the group of $0\text{--}10^2$ flux range, suggesting that we can select $100\text{ cm}^{-2}\text{ sr}^{-1}\text{ s}^{-1}$ (i.e., ~ 1 count/s) as the feasible threshold value of the trapped electron flux for the POES/FY-3 medium energy channel in our following analysis. While there still exist some conjunctions with the ratio >10 in groups of $10^2\text{--}10^3\text{ cm}^{-2}\text{ sr}^{-1}\text{ s}^{-1}$ and $10^3\text{--}10^4\text{ cm}^{-2}\text{ sr}^{-1}\text{ s}^{-1}$, the proportion of these data is tolerably small, say, $\sim 5\%$.

Fig. 4 shows the distribution of FY-3-to-POES electron flux ratio as a function of the POES flux. Notably, both panels show the apparent dominance of the ratio points

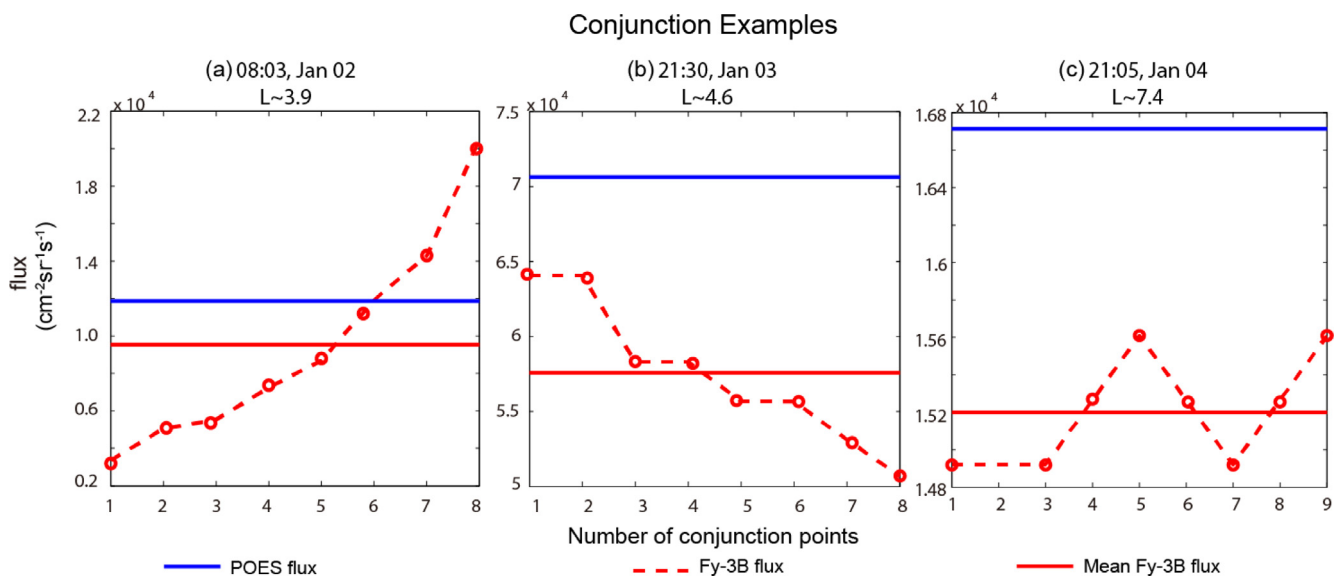


Fig. 2. Three randomly selected conjunction event examples between FY-3B and MetOp-02 within the bin size of ~ 0.5 MLT \times 0.1 L \times 5 min. The red dashed line represents the FY-3B 150–350 keV electron fluxes with the red solid line as the average value of these points. The blue solid line indicates the conjugate POES 100–300 keV electron trapped fluxes. (For interpretation of the references to colour in this figure legend, the reader is referred to the web version of this article.)

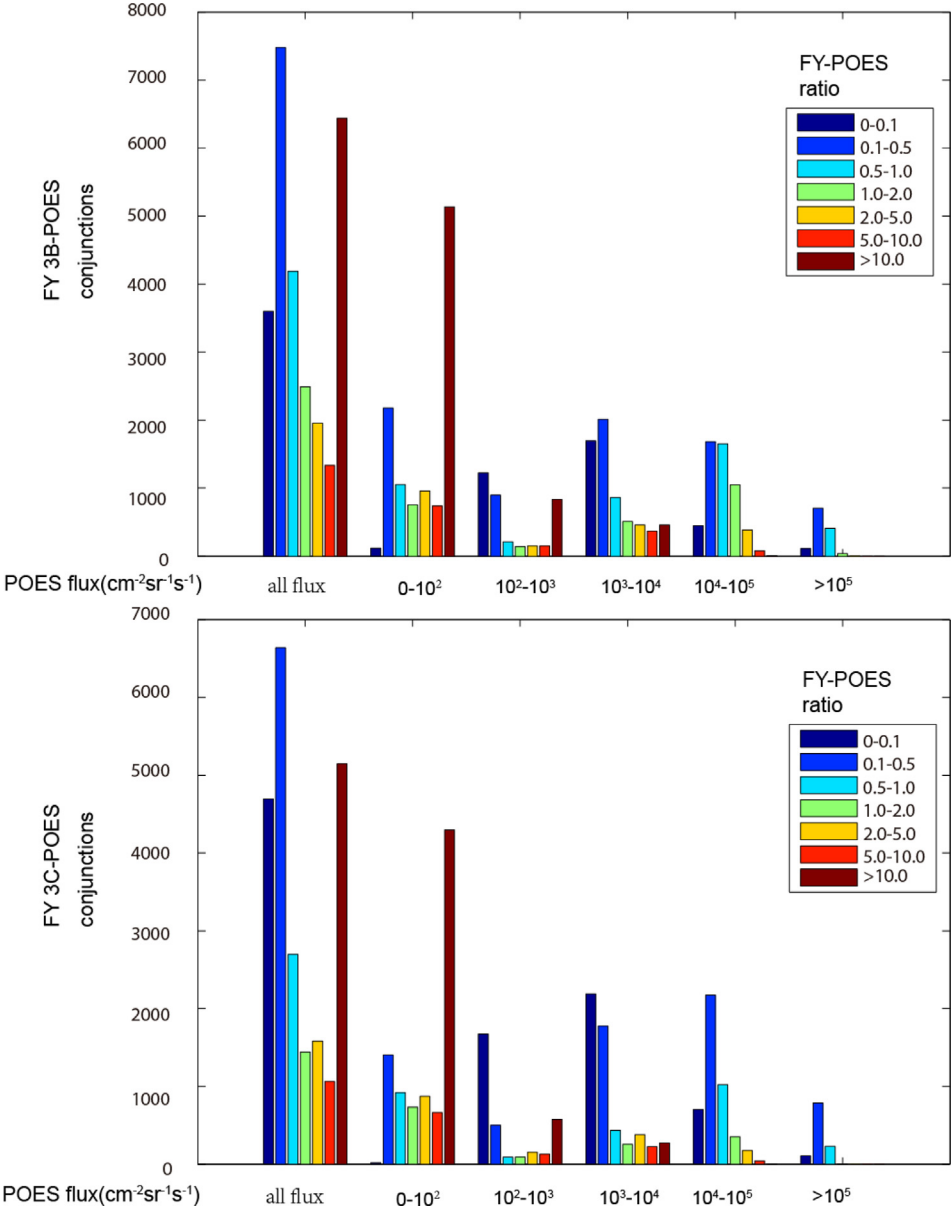


Fig. 3. Histograms showing the distribution of conjunction events as a function of the FY-3-to-POES flux ratio at different flux ranges of 100–300 keV electrons observed by POES.

within 0.1–10, which presents a good hint of systematic uncertainty. As a consequence, in order to obtain a relatively high-quality database, we nominally set two (one lower and one upper) boundary values of the ratio for further investigation. Specifically, the two horizontal red solid lines in each panel represent the adopted threshold levels, say 0.05–5 in Fig. 4(a) and 0.03–5 in Fig. 4(b), which help to retain more reliable points but avoid less certain data. By doing so, we finally register 11,359 and 9005 conjunction points with POES for FY-3B and 3C at L = 2–7, respectively.

3.2. Adjustment factors from inter-calibration

With the conjunction database described above, we can proceed to evaluate the systematic uncertainties associated

with the FY-3B and 3C flux measurements of the 150–350 keV electron channel. Since the number of selected data sets is actually very large at most target L-shells, it tends to be less appropriate to use the common least squares as a fitting method to explore the adjustment factors for different L-shell ranges. To better investigate the systematic differences between electron flux conjunctions, following Ni et al. (2011), we introduce the normalized differences (ND):

$$ND = \frac{flux1 - flux2}{(flux1 + flux2)/2} \times 100\%, \quad (1)$$

where $flux1$ and $flux2$ are electron fluxes obtained from the FY-3 and POES measurements, respectively. As shown from Fig. 5(a)–(d), we take the calibration case of FY-3B at L = 2–3 as an example to illustrate our inter-satellite

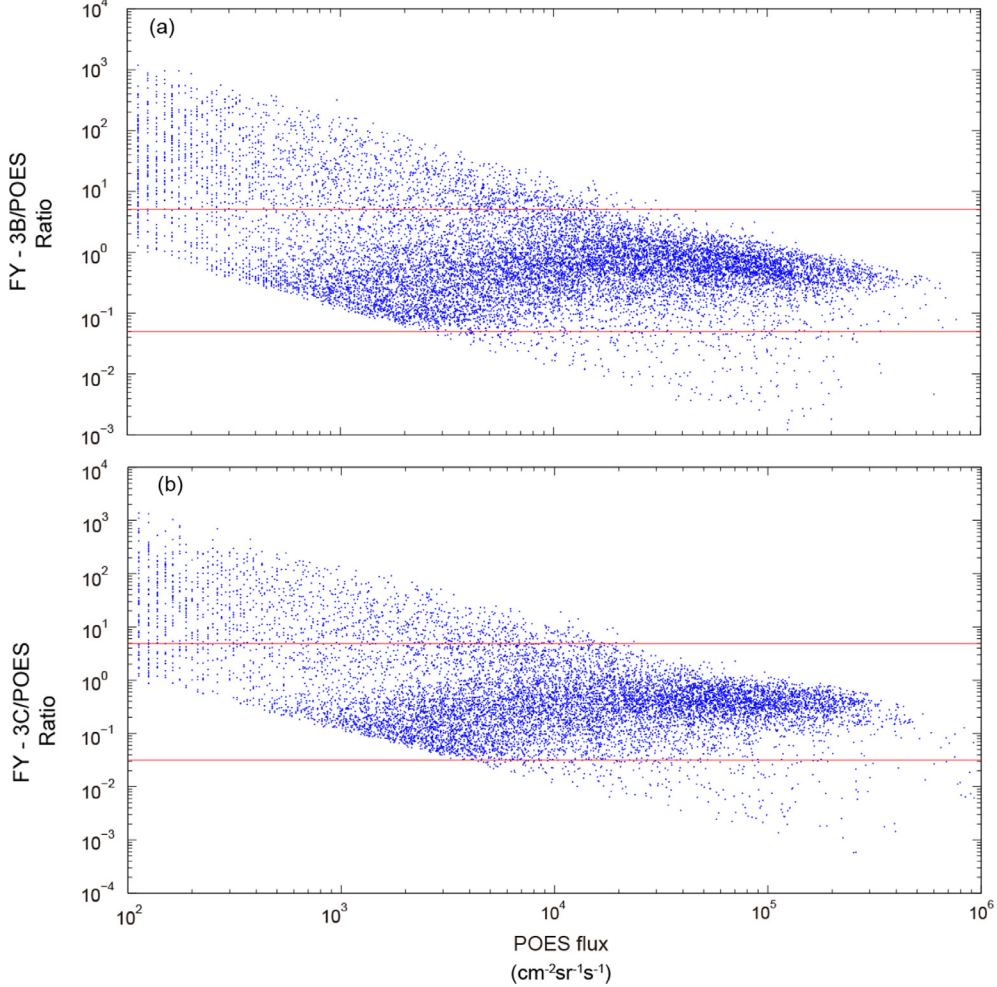


Fig. 4. Scatter plots of the FY-3-to-POES ratios as a function of the POES 100–300 keV electron flux. The two red solid lines in each panel represents the lower and upper threshold levels adopted for further data selection. (For interpretation of the references to colour in this figure legend, the reader is referred to the web version of this article.)

calibration procedure. Fig. 5(a) shows the identified flux conjunctions between FY-3B and POES. With the red¹ dashed diagonal line of slope = 1 that denote the perfect agreement between the two fluxes, we can see most of the conjunctive points are located below it, indicating that in general the FY-3B data for the 150–350 keV energy channel provide electron fluxes lower than the POES 100–300 keV electron fluxes at L = 2–3. Fig. 5(b) shows the histogram of *ND* which reveals a rough Gaussian distribution peaked $\sim -150\%$, suggesting that the FY-3B 150–350 keV electron fluxes should be systematically underestimated compared to the measurements at the 100–300 keV energy channel from POES. To quantify the systematic uncertainties, we subsequently multiply the FY-3 electron fluxes by an array of constant factor between 0.1 and 10, and select the specific value that minimizes the averaged absolute difference and standard deviation of the flux conjunctions for the satellite pair under investigation.

¹ For interpretation of color in ‘Fig. 5’, the reader is referred to the web version of this article.

As a result, we obtain the adjustment factor of 2.44 for the FY-3B – POES conjunction pair at L = 2–3. The corresponding scatter plot of the electron flux conjunctions and the *ND* histogram after the inter-satellite calibration are shown in Fig. 5(c) and (d), respectively. Apparently, the distribution of the flux conjunction exhibits a typical Gaussian variation around *ND* = 0, demonstrating a reasonable calibration for the FY-3B 150–350 keV channel with POES electron measurements. Following the same procedure, we investigate the *ND* histograms and evaluate the intercalibration factors for various pairs of both FY-3 probes and POES satellites at higher L-shell ranges in the inner magnetosphere, the results of which are shown in Figs. 6–9.

Notably, most FY-3-POES flux conjunctions show good agreement with each other, indicating that the systematic uncertainties associated with the FY-3 150–350 keV electron flux are largely reduced or removed. The obtained adjustment factors are listed in Table 1 as tabulated for FY-3B and FY-3C for five indicated L-shell ranges. Compared to the POES 100–300 keV electron flux data,

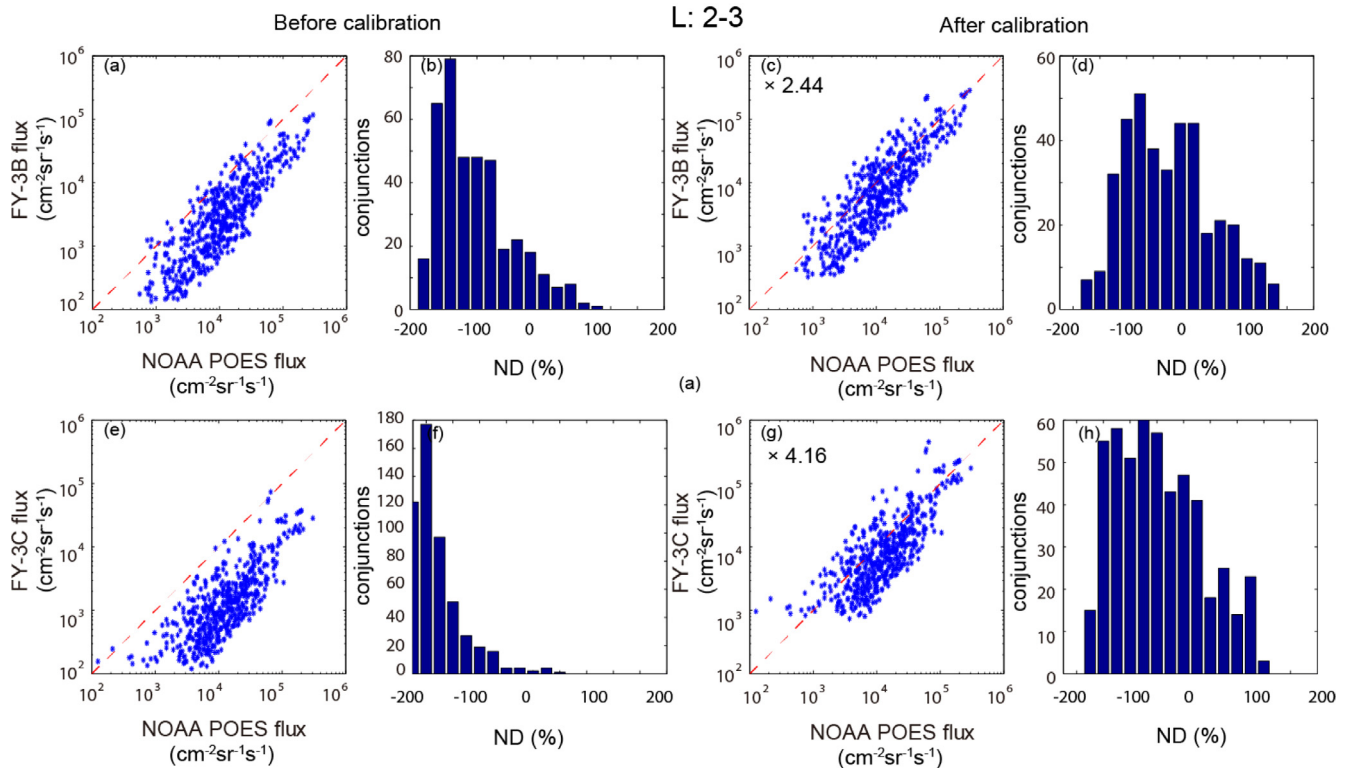


Fig. 5. Distributions of (top) FY-3b and (bottom) FY-3C electron flux conjunctions at $L = 2-3$ with normalized differences (ND) before and after inter-satellite calibration.

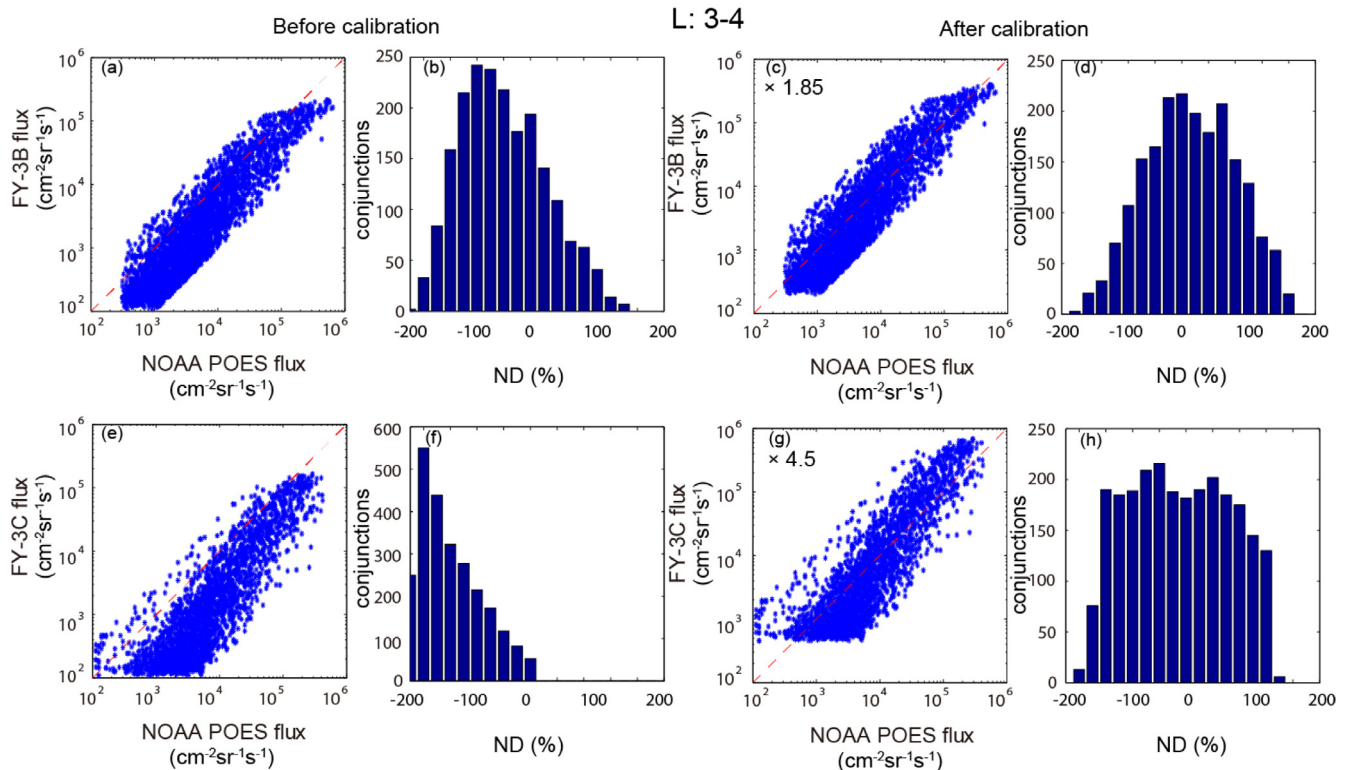


Fig. 6. Same as in Fig. 5, except for $L = 3-4$.

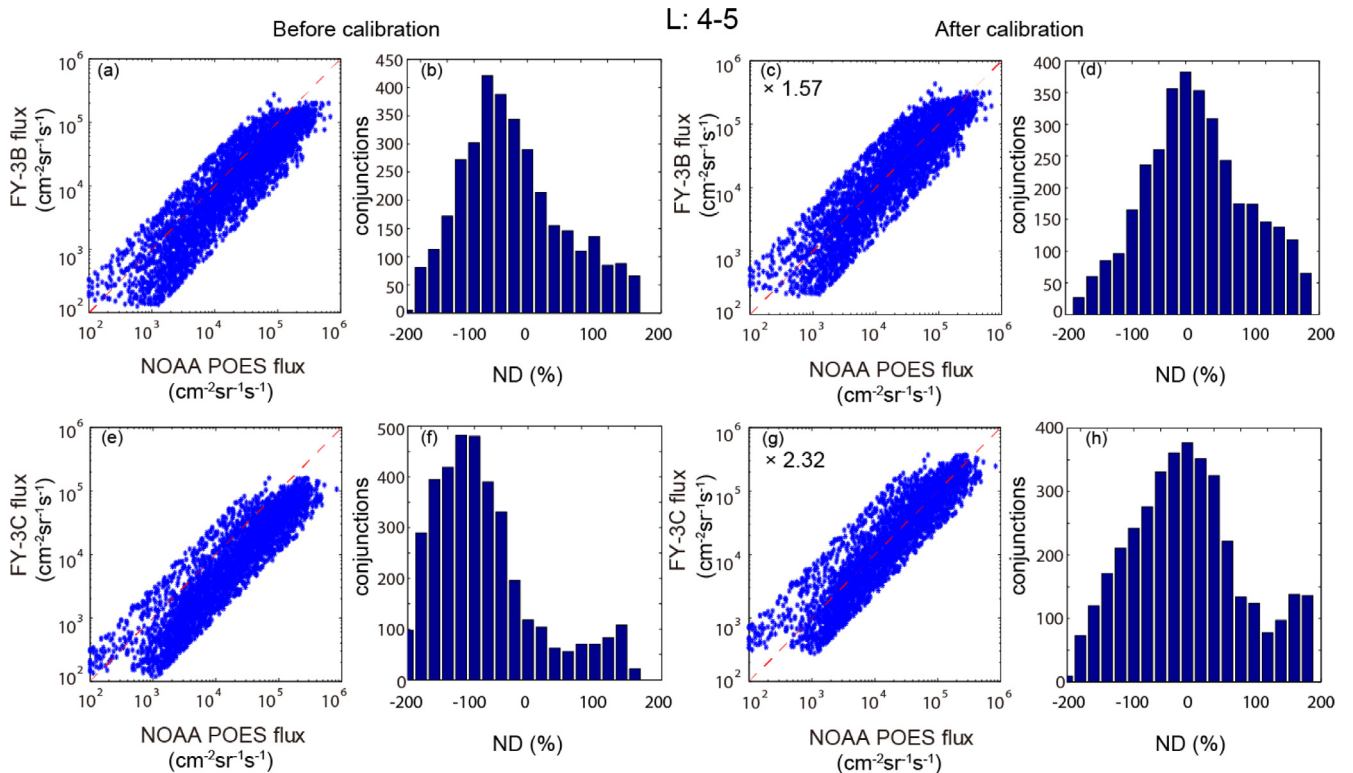


Fig. 7. Same as in Fig. 5, except for L = 4–5.

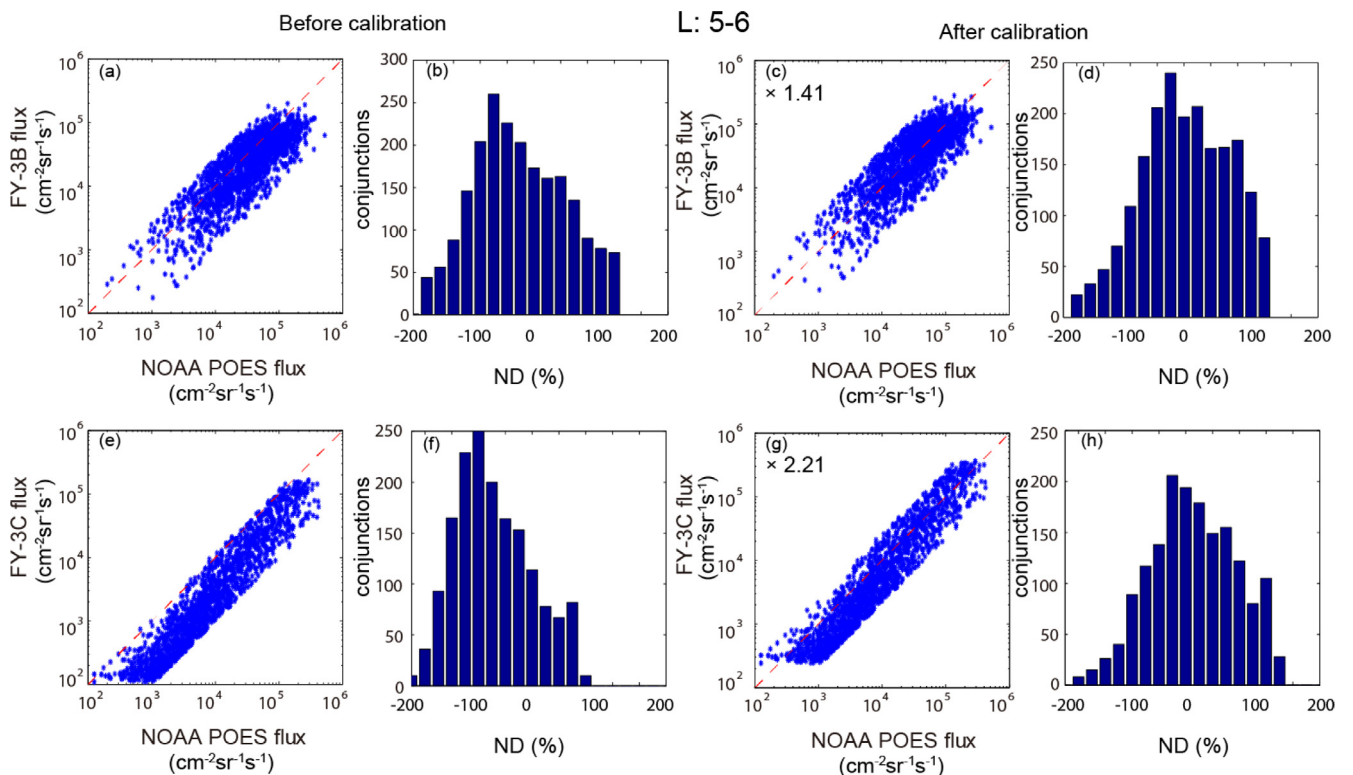


Fig. 8. Same as in Fig. 5, except for L = 5–6.

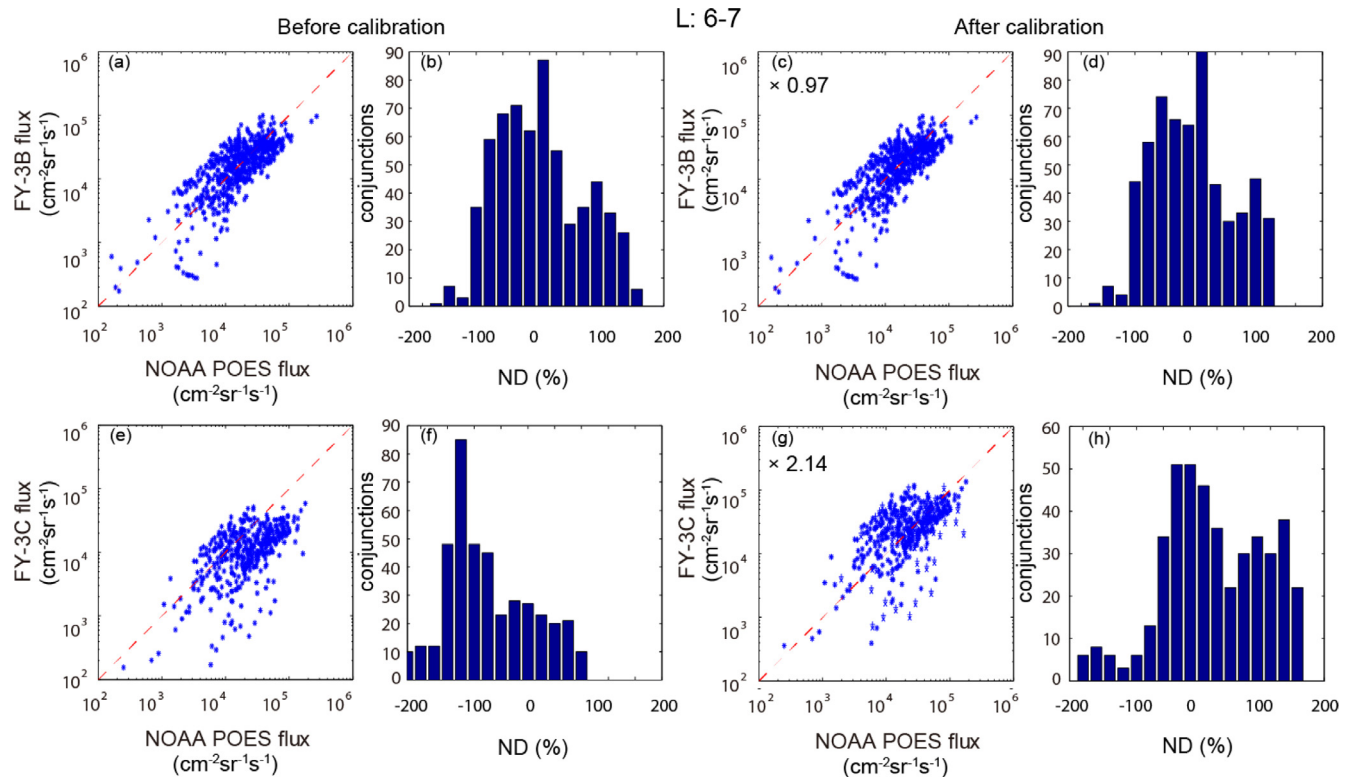
Fig. 9. Same as in Fig. 5, except for $L = 6-7$.

Table 1

Inter-satellite calibration factors for FY-3B and FY-3C electron flux measurements as a function of L-shell range based on flux conjunctions with NOAA POES electron data.

Adjustment factors based on inter-satellite calibration

	$L = 2-3$	$L = 3-4$	$L = 4-5$	$L = 5-6$	$L = 6-7$
FY-3B	2.44	1.85	1.57	1.41	0.97
FY-3C	4.16	4.5	2.32	2.21	2.14

the FY-3 150–350 keV electron data tend to underestimate the trapped medium-energy electron fluxes within a factor of 5 under most circumstances. It is also indicated in Table 1 that the adjustment factors for FY-3C are consistently larger than those for FY-3B at each L shell range, within a factor of 2.5, demonstrating that the detector onboard FY-3B tends to produce more reliable flux information of 150–350 keV electrons.

4. Conclusive remarks

In the present study we have performed a useful inter-satellite calibration analysis of FY-3B and FY-3C trapped medium energy electron fluxes with NOAA POES electron measurements, based on physical conjunctions for a whole year of 2014. The FY-3 trapped electron flux data, together with the POES (including NOAA POES 15, 16, 18, 19 and MetOp-02) electron flux data, have been adopted to quantify the systematic uncertainties between the sun-

synchronous orbit satellite pairs for different L shell ranges between $L = 2-7$. By defining rough conjunctions within the bin size of $\sim 0.5 \text{ MLT} \times 0.1 \text{ L} \times 5 \text{ min}$, we have collected a robust database of electron flux conjunctions for detailed investigation.

Compared to the POES data, the FY-3B and FY-3C data generally exhibit a similar trend of electron flux variations but more or less underestimate them within a factor of 5 for the medium electron energy 150–350 keV channel. The obtained adjustment factors (i.e., the cross-satellite calibration factor) for FY-3C are consistently larger than those for FY-3B at each L-shell range, within a factor of 2.5, demonstrating that the detector onboard FY-3B tends to produce more reliable flux information of 150–350 keV electrons. Good consistency in the flux conjunctions after the inter-calibration procedures gives us certain confidence to generalize our method to calibrate electron flux measurements from various satellite instruments.

Meanwhile, as L-shell increases, the systematic uncertainties follow a generally decreasing trend for both FY-3 probes. This may result from various impacts from both the natural particle radiation environment and the satellite detector capabilities, which requires future investigation but is outside the scope of the present study.

Evidently, incorporation of reliable L-dependent inter-satellite calibration factors (i.e., Table 1) into the original FY-3 medium energy electron fluxes can help reduce or remove the major systematic uncertainties associated with the measurements. Therefore, based on the cross-satellite

calibration procedure, we can establish a reasonably improved FY-3B and FY-3C database of radiation belt medium energy (i.e., 150–350 keV) electron fluxes, which can be then adopted for future investigation upon the radiation belt electron dynamics.

Acknowledgements

This work was supported by the NSFC grants 41674163, 41204120, 41474141, 41304130 and 41574160, the Project Supported by the Specialized Research Fund for State Key Laboratories, the Projects funded by China Postdoctoral Science Foundation (2013M542051 and 2014T70732), and the Hubei Province Natural Science Excellent Youth Foundation (2016CFA044). The authors thank China Meteorological Administration and National Space Science Center for provision of the FengYun 3 data.

References

- Baker, D.N., Jaynes, A.N., Hoxie, V.C., Thorne, R.M., Foster, J.C., Li, X., 2014. An impenetrable barrier to ultrarelativistic electrons in the Van Allen radiation belts. *Nature* 515 (7528), 531–534.
- Cao, X., Shprits, Y., Ni, B., Zhelavskaya, I.S., 2017. Scattering of ultra-relativistic electrons in the Van Allen radiation belts accounting for hot plasma effects. *Sci. Rep.* 7, 17719. <https://doi.org/10.1038/s41598-017-17739-7>.
- Casadio, S., Arino, O., 2011. Monitoring the South Atlantic anomaly using ATSR instrument series. *Adv. Space Res.* 48, 1056–1066.
- Cayton, T.E., Tuszezski, M., 2005. Revised electron fluxes from the synchronous orbit particle analyzer. *Space Weather*. <https://doi.org/10.1029/2005SW000150>.
- Chen, Y., Friedel, R.H.W., Reeves, G.D., Onsager, T.G., Thomsen, M.F., 2005. Multi-satellite determination of the relativistic electron phase space density at geosynchronous orbit: methodology and results during geomagnetically quiet times. *J. Geophys. Res.: Space Phys.* 110 (A10).
- Evans, D.S., Greer, M.S., 2004. Polar Orbiting Environmental Satellite Space Environment Monitor-2: Instrument Descriptions and Archive Data Documentation Archive Data Documentation, NOAA Tech. Mem. 93, Version 1.4, Space Weather Predict. Cent., Boulder, Colo.
- Friedel, R.H.W., Reeves, G.D., Obara, T., 2002. Relativistic electron dynamics in the inner magnetosphere – a review. *J. Atmos. Sol.-Terr. Phys.* 64 (2), 265–282.
- Friedel, R.H.W., Bourdarie, S., Cayton, T.E., 2005. Intercalibration of magnetospheric energetic electron data. *Space Weather* 3 (9).
- Green, J.C., 2013. MEPED Telescope Data Processing Algorithm Theoretical Basis Document, Natl. Oceanic and Atmos. Admin Space Environmental Cental, Boulder, CO.
- Huang, C., Li, J., Yu, T., Xue, B., Wang, C., Zhang, X., Cao, G., Liu, D., Tang, W., 2012. The capabilities and applications of FY-3A/B SEM on monitoring space weather events. *IEEE Trans. Geosci. Rem. Sens.* 50 (12), 4975–4985.
- Lam, M.M., Horne, R.B., Meredith, N.P., Glauert, S.A., Moffat-Griffin, T., Green, J.C., 2010. Origin of energetic electron precipitation > 30 keV into the atmosphere. *J. Geophys. Res.* 115, A00F08. <https://doi.org/10.1029/2009JA014619>.
- Li, J., Huang, C., Yu, C., Zhang, X., Wang, C., Zhang, X., Cao, G., Sun, Y., et al., submitted for publication. Calibration and applications of FY-3C SEM high energy particle data. *J. Astronaut.* (submitted for publication) (in Chinese)
- Li, W., Ni, B., Thorne, R.M., Bortnik, J., Green, J.C., Kletzing, C.A., Kurth, W.S., Hospodarsky, G.B., 2013. Constructing the global distribution of chorus wave intensity using measurements of electrons by the POES satellites and waves by the Van Allen Probes. *Geophys. Res. Lett.* 40, 4526–4532. <https://doi.org/10.1002/grl.50920>.
- Meredith, N.P., Horne, R.B., Lam, M.M., Denton, M.H., Borovsky, J.E., Green, J.C., 2011. Energetic electron precipitation during high-speed solar wind stream driven storms. *J. Geophys. Res.* 116, A05223. <https://doi.org/10.1029/2010JA016293>.
- Ni, B., Shprits, Y., Nagai, T., Thorne, R., Chen, Y., Kondrashov, D., Kim, H.J., 2009a. Reanalyses of the radiation belt electron phase space density using nearly equatorial CRRES and polar-orbiting Akebono satellite observations. *J. Geophys. Res.: Space Phys.* 114 (A5).
- Ni, B., Shprits, Y., Thorne, R., Friedel, R., Nagai, T., 2009b. Reanalysis of relativistic radiation belt electron phase space density using multisatellite observations: sensitivity to empirical magnetic field models. *J. Geophys. Res.: Space Phys.* 114 (A12).
- Ni, B., Shprits, Y., Hartinger, M., Angelopoulos, V., Gu, X., Larson, D., 2011. Analysis of radiation belt energetic electron phase space density using THEMIS SST measurements: cross-satellite calibration and a case study. *J. Geophys. Res.: Space Phys.* 116 (A3).
- Ni, B., Bortnik, J., Thorne, R.M., Ma, Q., Chen, L., 2013. Resonant scattering and resultant pitch angle evolution of relativistic electrons by plasmaspheric hiss. *J. Geophys. Res.: Space Phys.* 118 (12), 7740–7751.
- Ni, B., Li, W., Thorne, R.M., Bortnik, J., Green, J.C., Kletzing, C.A., Kurth, W.S., Hospodarsky, G.B., Soria-Santacruz Pich, M., 2014. A novel technique to construct the global distribution of whistler mode chorus wave intensity using low-altitude POES electron data. *J. Geophys. Res. Space Phys.* 119, 5685–5699. <https://doi.org/10.1002/2014JA019935>.
- Ni, B., Cao, X., Zou, Z., Zhou, C., Gu, X., 2015. Resonant scattering of outer zone relativistic electrons by multiband EMIC waves and resultant electron loss time scales. *J. Geophys. Res.: Space Phys.* 120 (9), 7357–7373.
- Ni, B., Cao, X., Shprits, Y.Y., Summers, D., Gu, X., Fu, S., Lou, Y., 2018. Hot plasma effects on the cyclotron-resonant pitch-angle scattering rates of radiation belt electrons due to EMIC waves. *Geophys. Res. Lett.* 45. <https://doi.org/10.1002/2017GL076028>.
- Olson, W.P., Pfitzer, K.A., 1977. Magnetospheric Magnetic Field Modeling. Annual Scientific Report. AFOSR Contract F44620-75-C-0033. McDonnell Douglas Astronaut. Co., Huntington Beach, Calif.
- Reeves, G.D., McAdams, K.L., Friedel, R.H.W., O'Brien, T.P., 2003. Acceleration and loss of relativistic electrons during geomagnetic storms. *Geophys. Res. Lett.* 30 (10).
- Rodger, C.J., Clilverd, M.A., Green, J.C., Lam, M.M., 2010. Use of POES SEM-2 observations to examine radiation belt dynamics and energetic electron precipitation into the atmosphere. *J. Geophys. Res.* 115, A04202. <https://doi.org/10.1029/2008JA014023>.
- Thorne, R.M., Horne, R.B., Glauert, S., Meredith, N.P., Shprits, Y.Y., Summers, D., Anderson, R.R., 2005. The influence of wave-particle interactions on relativistic electron dynamics during storms. In: Inner Magnetosphere Interactions: New Perspectives from Imaging, pp. 101–112.
- Thorne, R.M., 2010. Radiation belt dynamics: the importance of wave-particle interactions. *Geophys. Res. Lett.* 37, L22107. <https://doi.org/10.1029/2010GL1044990>.
- Thorne, R.M., Li, W., Ni, B., Ma, Q., Bortnik, J., Chen, L., Baker, D.N., Spence, H.E., Reeves, G.D., Henderson, M.G., Kletzing, C.A., Kurth, W.S., Hospodarsky, G.B., Blake, J.B., Fennell, J.F., Claudepiere, S. G., Kanekal, S.G., 2013. Rapid local acceleration of relativistic radiation-belt electrons by magnetospheric chorus. *Nature* 504, 411–414. <https://doi.org/10.1038/nature12889>.
- Wang, C., Zhang, X., Wang, S., Wang, Y., Liu, C., Jin, T., 2010. Comparisons of high energy particles observation results between FY-3A satellite and NOAA series satellites. *Chin. J. Space Sci.* 30, 49–54.
- Wang, C., Zhang, X., Li, J., Huang, C., Zhang, X., Jing, T., Shen, G., Zhang, S., Cao, G., Sun, Y., Liang, J., Zhu, G., Han, Y., 2013. Cross-calibration of high energetic particles data – a case study between FY-3B and NOAA-17. *Sci. China Tech. Sci.* 56, 2688–2674, 10 1007/s11431-013-5375-2.

- Xiang, Z., Ni, B., Zhou, C., Zou, Z., Gu, X., Zhao, Z., 2016. Multi-satellite simultaneous observations of magnetopause and atmospheric losses of radiation belt electrons during an intense solar wind dynamic pressure pulse. *Ann. Geophys.* 34, 493–509. <https://doi.org/10.5194/angeo-34-493-2016>.
- Xiang, Z., Tu, W., Li, X., Ni, B., Morley, S.K., Baker, D.N., 2017. Understanding the mechanisms of radiation belt dropouts observed by Van Allen Probes. *J. Geophys. Res.: Space Phys.* 122. <https://doi.org/10.1002/2017JA024487>.